

# Pore Structure and Fractal Dimension in Marine Mature Silicon-Rich Shale of the Dalong Formation in Western Hubei

Weiqing Liu,\* Qiang Zhu, Yu Qiao, Jienan Pan, Wei Wu, and Luqi Chen

Cite This: *ACS Omega* 2024, 9, 11718–11729

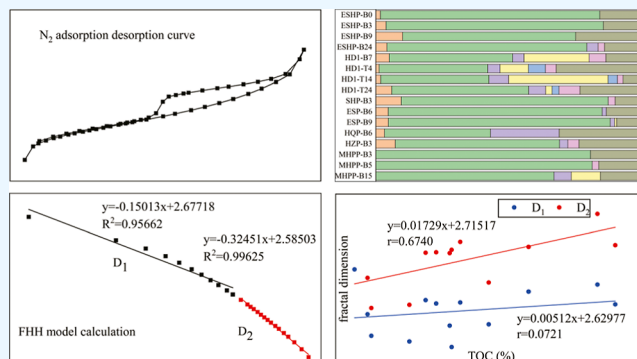
Read Online

ACCESS |

Metrics &amp; More

Article Recommendations

**ABSTRACT:** How shale reservoirs and gas contents are affected by the pore structure of shale is very important. Low-temperature nitrogen isothermal adsorption experiments were conducted by us to investigate the pore structure of the Dalong Formation shale. We measured the specific surface area and fractal dimension of the pores and also considered the mineral fraction and organic matter content of the rock. The results show that the Dalong Formation shale contains a lot of organic carbon, with a total organic carbon (TOC) value between 1.20 and 10.82% (mean: 5.02%). Quartz and clay minerals are the main components of the shale, with quartz making up 40.30 to 85.60% (mean: 67.21%) and clay minerals making up 9.20 to 34.10% (mean: 20.26%) of the shale. Most of the pore space in the shale of the Dalong Formation is formed by intragranular and intergranular pores, organic matter pores, and some microfissures. The pore structure is complex, with parallel-plate and ink-bottle pores being the most common types. Most of the pores are 0–2 or 2–5 nm in size.  $D_1$  and  $D_2$  are the fractal dimensions, with averages of 2.66 and 2.81, respectively.  $D_1$  can range from 2.55 to 2.78, while  $D_2$  can range from 2.66 to 2.94. The TOC content, mineral composition, and pore structure characteristics determine the fractal dimension. Higher levels of the TOC content, quartz mineral content, and specific pore surface area result in a higher fractal dimension, while higher levels of feldspar content result in a lower one. There is no apparent correlation to clay minerals or other mineral compositions.



## 1. INTRODUCTION

Shale gas is an important renewable energy source with low carbon emissions, high efficiency, and wide applications.<sup>1,2</sup> As the global economy and technology advance, shale gas research and development has become a prominent topic in the energy sector. Shale gas has the unique property of self-generation and self-storage,<sup>3,4</sup> as shale acts as both a hydrocarbon source rock and a reservoir layer.<sup>5</sup> Shale gas reservoir research requires a good understanding of the shale pore structure. Various laboratory testing technologies and experimental methods have been used to characterize shale pore structure,<sup>6–8</sup> including scanning electron microscopy (SEM), nano-computed tomography, high-pressure mercury injection, gas adsorption ( $N_2$  and  $CO_2$ ), nuclear magnetic resonance, and neutron small-angle scattering.

The complex and heterogeneous pore structure of shale poses challenges for characterization. However, the fractal dimension provides a quantitative approach to describe this characteristic. Fractal dimension was initially introduced by B.B. Mandelbrot for studying the coastline of Britain and has since been applied to various scientific fields.<sup>9</sup> The pore structure of shale was investigated by Avnir and Krohn using molecular adsorption and SEM techniques, and they discovered its fractal features.<sup>10,11</sup> The pore structure of coal and sandstone is described by fractal

theory, which is an effective method.<sup>12,13</sup> In the study of shale pores, scholars are increasingly applying the fractal theory. Calculation methods for the fractal dimension of shale pores include Frenkel–Halsey–Hill (FHH), Newton–Kantorovich (NK), and Wang–Li (WL) models.<sup>14–17</sup> The FHH model combined with nitrogen adsorption data is commonly used due to its simplicity and reliable results.<sup>18–22</sup>

China possesses abundant shale gas resources. It is mainly concentrated in the Longmaxi Formation in the Sichuan Basin and its periphery. This is where China's shale gas development is focused.<sup>23</sup> The successful drilling of shale gas in the Dalong Formation shale in western Hubei suggests that it is a potential new area for exploration and development.<sup>24</sup> A muddy silica shale mainly makes up the Longmaxi Formation shale, which has 44.5% quartz and 34.7% clay minerals on average.<sup>25–28</sup> The silica content of the Dalong Formation shale is higher (59.8% on

Received: November 16, 2023

Revised: December 21, 2023

Accepted: February 13, 2024

Published: February 26, 2024



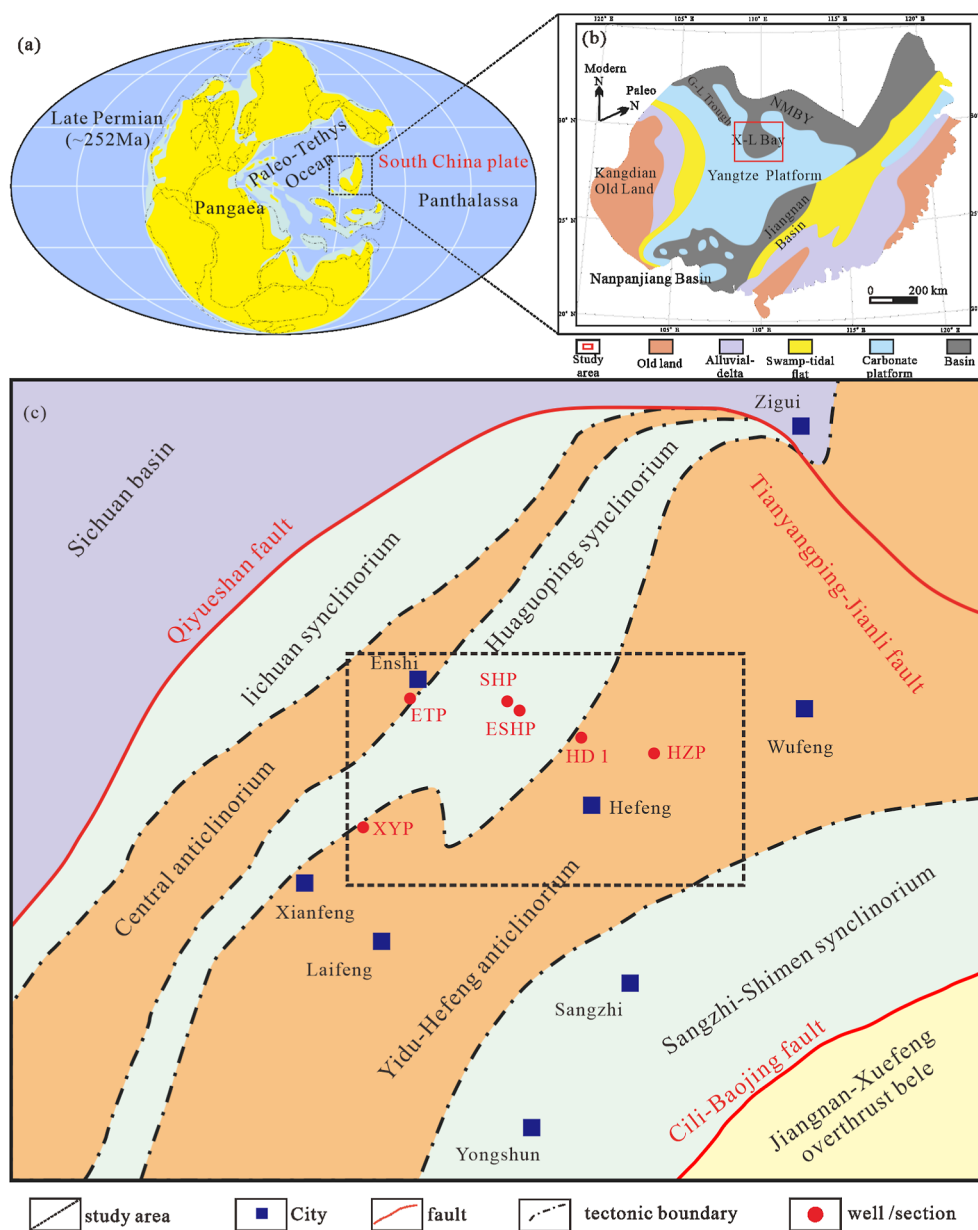


**Figure 1.** (a) Late Permian global paleogeographic map [adapted with permission from ref 38 Copyright (2017) (Elsevier)] and (b) late Permian lithofacies paleogeography of the South China plate [adapted with permission from ref 39 Copyright (2023) (Elsevier)]. (c) Modern tectonic map of western Hubei [adapted with permission from ref 40 Copyright (2020) (Elsevier)].

average) and the clay minerals are lower (16.6% on average) than the Longmaxi Formation shale.<sup>29–31</sup> The Dalong Formation silica shale has been studied for its geochemical features, depositional setting and reservoir properties in previous research,<sup>32,33</sup> and according to Wu et al., the Dalong Formation has a high amount of quartz that originated from living organisms.<sup>34</sup> The effects of abundant siliceous minerals and scarce clay minerals on the Dalong Formation shale reservoir features are still unclear.

In this study, the western Hubei shale of the Dalong Formation is investigated. Using low-temperature nitrogen isothermal adsorption experiments, we study the pore structure of the shale, combined with petrology, organic and inorganic geochemistry tests, and SEM observations. We calculate the fractal dimension of shale pores by the FHH model and examine its factors. Our results can offer useful guidance for shale gas exploration and development in our region.

## 2. GEOLOGICAL SETTING

The West Hubei Basin was formed during the middle to late Permian period. At that time, the South China plate, located in the western part of Pangaea near the Palaeoequator, faced the Palaeotethys Ocean in the east<sup>35,36</sup> (Figure 1a). Before the basin formed, the crust in western Hubei experienced uplift and erosion during the early late Carboniferous period, resulting in the majority of the area becoming land. In the early Permian period, a marine transgression occurred, creating a clastic coastal environment that gradually transformed into a restricted carbonate platform sea during the middle to late Permian period. The formation of the basin ceased in the late Permian period when the crust experienced another round of uplift and erosion. Subsequently, in the early Triassic period, the basin was flooded by seawater, forming a clastic coastal area.<sup>37</sup>

Table 1. X-ray Diffraction Mineral Analysis Results and TOC Content of the Dalong Formation Shale

sample	TOC %	quartz %	plagioclase %	calcite %	dolomite%	pyrite %	clay %
ESHP-B0	1.68	82.10					17.90
ESHP-B3	3.82	83.10					16.90
ESHP-B9	10.82	69.90	1.00				29.10
ESHP-B24	4.21	76.80	4.30			2.50	16.50
HD1-B7	5.10	47.80	4.40	25.20		6.50	16.10
HD1-T4	1.20	40.50	4.60	10.60	6.30	4.00	34.10
HD1-T14	1.82	40.60	7.40	37.30	3.50	2.10	9.20
HD1-T24	6.15	53.50	6.60	2.50	2.70	8.20	26.40
SHP-B3	10.16	83.20	1.00			2.80	13.00
ESP-B6	4.71	82.50	1.60				15.90
ESP-B9	4.78	85.60	1.70	0.80			11.90
HQP-B6	3.22	40.30	26.10				33.60
HZP-B3	7.62	65.10	3.30			4.40	27.20
MHPP-B3		79.00					21.00
MHPP-B5		79.70				2.40	18.00
MHPP-B15		65.60	6.40	10.70			17.40

The West Hubei Basin was enclosed by platforms on three sides and linked to the wide ocean by a thin sea inlet in the north during the late Permian. This created a semiclosed sedimentary environment (Figure 1b).<sup>41</sup> The West Hubei Basin was a residual basin that underwent reconstruction and superimposition by various types of prototypical basins.<sup>42</sup> Unlike other areas of South China dominated by carbonate rocks, the sediments in the West Hubei Basin mainly consisted of deep-water silica-rich shale of the Dalong Formation.<sup>36</sup> The main lithologies in the basin included silica-rich mudstone, argillaceous lime mudstone,<sup>34,43</sup> and organic-rich mudstone. These gradually transformed into Permian limestone from the center to the surrounding platforms.<sup>41,44</sup>

The study region lies in the middle of the Western Hunan–Hubei fold fault zone, adjacent to the Sichuan Basin.<sup>45</sup> Strong deformation occurred in the area due to the Yanshan fold movement at the end of the Jurassic, resulting in a northeast-oriented fold and fault structure (Figure 1c). There are three main faults around the study area: the Qiyueshan fault in the northwest, the Tianyangping-Jianli fault in the northeast, and the Cili-Baojing fault in the southeast. The geological tectonic units in the study area are as follows from the northwest to southeast: Lichuan synclinorium, central anticlinorium, Huangoping synclinorium, Yidu-Hefeng anticlinorium, Sangzhi-Shimen synclinorium, and Jiangnan Xuefeng nappe uplift in the southeast.

### 3. SAMPLES AND METHODS

This study analyzed 16 shale samples from the section and drilling of the Dalong Formation in western Hubei. Among them, HD1-B7 (1281.5 m), HD1T4 (1246.52–1246.62 m), HD1-T14 (1260.71–1260.79 m), and HD1-T24 (1273.60–1273.71 m) were collected in well HD1, and the remaining samples were collected in outcrops. The microstructure components of the samples were observed using an optical microscope and SEM. SEM analysis was performed at the SGS (Beijing) laboratory. The instrument used was an FEI-200 F scanning electron microscope, and the method followed was the SY/T5162-2014 analysis method. The samples were observed in secondary electron and backscattered modes.

X-ray diffraction was used to analyze the mineral composition of the samples. The American Leco CS230 carbon and sulfur analyzer was used to measure the total organic carbon (TOC)

content of the samples. The sample preparation involved crushing and sieving, placing it in a sample bag, and labeling it. To convert the TOC to carbon dioxide, the sample was burned in a high-temperature oxygen flow after removal of the inorganic carbon with dilute hydrochloric acid. An infrared detector was used to detect the TOC content.

To characterize the pore structure parameters of shale, a low-temperature nitrogen adsorption experiment was performed. The experimental instrument was an Autosorb-IQ3. Before the experiment, the sample was ground to 60 mesh by using agate. To remove moisture, the sample was dried at 110 °C for 12 h in a vacuum environment. Then, at a temperature of 77.4 K and a relative pressure range of 0.010–0.998, a low-temperature nitrogen adsorption experiment was performed. By applying the nonlocal density functional theory (NLDFT) method to the nitrogen adsorption results, the pore specific surface area (SSA), pore volume, and pore size distribution are calculated. The NLDFT model is calculated by SAIEUS software. The analytical models are carbon-N<sub>2</sub> NLDFT standard slit. The FHH model is applied to calculate the fractal dimension.

## 4. RESULTS

**4.1. TOC and Mineral Components.** Despite undergoing major tectonic shifts throughout its history, the Dalong Formation still has a lot of TOC in its shale samples. The TOC levels varied from 1.20 to 10.82% with a mean of 5.02%. The minerals in the samples were identified by X-ray diffraction, and the findings are in Table 1. Quartz and clay minerals are the dominant minerals in the shale samples from the Dalong Formation, with minor amounts of calcite, dolomite, pyrite, and feldspar. The quartz levels varied from 40.30 to 85.60%, with a mean of 67.21%, and the clay mineral levels varied from 9.20 to 34.10%, with a mean of 20.26%. The pyrite content had an average of 4.11%.

**4.2. Pore Morphology from SEM.** Shale reservoirs' physical properties are primarily influenced by pore types and structural characteristics, which can be observed using SEM. Scholars have proposed different classification schemes for shale pores, with the most widely used being the three-end member classification scheme by Loucks in 2012. This scheme categorizes pores into intra-, inter-, and organic pores. All three kinds of pores are found in the Dalong Formation shale, as shown by SEM analysis of the matrix pores and particles.

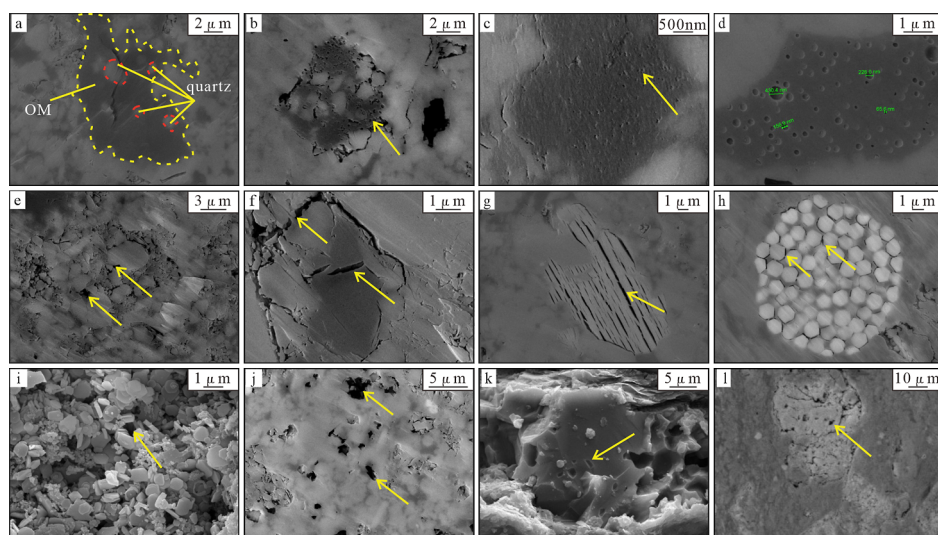


**Figure 2.** Pore morphology of the Dalong Formation shale: (a) organic matter is filled in intergranular pores; (b) organic matter encapsulates mineral particles and develops organic matter pores inside; (c) nanoscale micropores in organic matter; (d) smooth pores inside the organic matter; (e) intergranular pores of minerals; (f) intergranular pores of mineral particles and internal cracks of organic matter; (g) lamellar minerals and their interlamellar gaps; (h) intergranular pores of pyrite and pyrite minerals; (i) kaolinite intercrystalline pore of clay mineral; (j) dissolution pores; (k) internal dissolution pores of siliceous minerals; (l) internal dissolution pores of iron minerals.

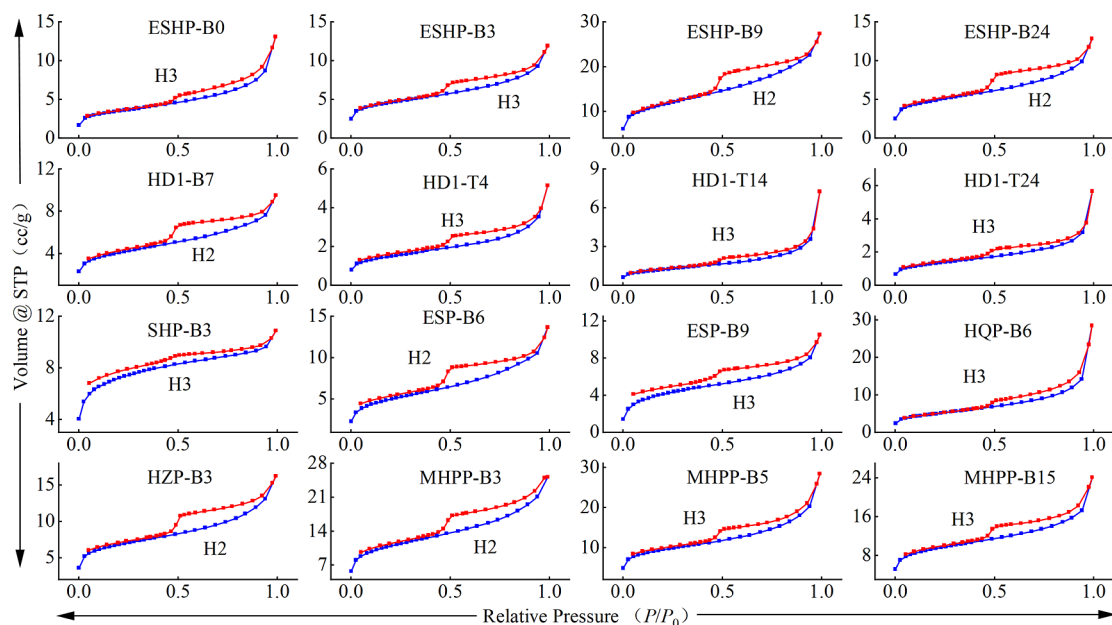


**Figure 3.**  $N_2$  adsorption–desorption isotherms for shales of the Dalong Formation.

The silica shale of the Dalong Formation contains a lot of organic matter, and SEM observations show that a significant amount of organic matter is deposited between mineral particles (Figure 2a) or encapsulated by them (Figure 2b). Nanometer-scale pores are abundant in the organic matter, primarily resulting from the thermal decomposition of organic matter during diagenesis. This decomposition generates gases and liquids that leave behind pores.<sup>46</sup> The Dalong Formation shale has organic pores of different sizes and shapes, such as bubble-like (Figure 2d) and crack-like (Figure 2f).

Intergranular pores mainly develop between some rigid minerals (such as quartz) and minerals that have been recrystallized during diagenesis. Quartz, as a rigid mineral, can preserve its pores during diagenesis due to its high compressive strength (Figure 2e). Mineral layers with a slice-like shape

(Figure 2g) and pores between pyrite crystals with an irregular or stripe-like shape (Figure 2h) are also observed. In addition, there are small amounts of pores between the kaolinite crystals (Figure 2i).

Diagenetic dissolution commonly generates dissolution pores in brittle minerals like quartz, feldspar, calcite, and dolomite.<sup>47</sup> The shale of the Dalong Formation contains a limited quantity of carbonate minerals, which are susceptible to dissolution during diagenesis, resulting in the formation of dissolution pores (Figure 2j). Additionally, dissolution pores are observed in siliceous minerals (Figure 2k) and a small amount of iron minerals (Figure 2l).

**4.3. Analysis Result of  $N_2$  Adsorption.** The nitrogen adsorption and desorption curves of the shale of the Dalong Formation are shown in Figure 3. The International Union of

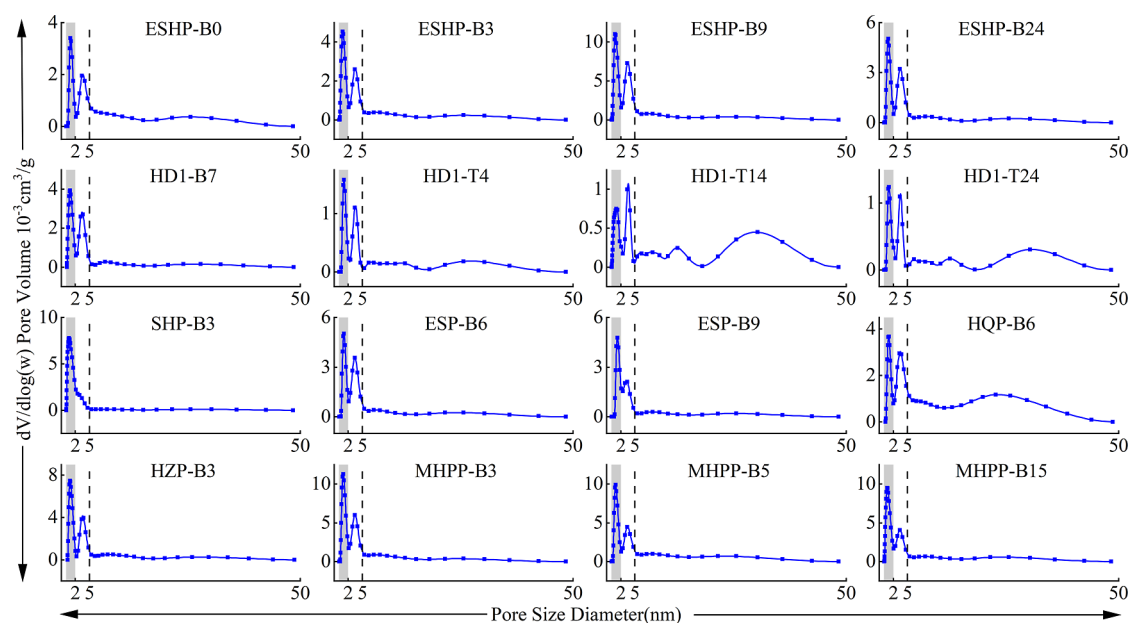


Figure 4. Pore size distribution curve of the Dalong Formation shale.

Table 2. Pore SSA and Volume Distribution of Shales in the Dalong Formation

sample	pore volume ( $\text{cm}^3 \cdot \text{g}^{-1} \times 10^{-3}$ )			pore SSA ( $\text{m}^2 \cdot \text{g}^{-1}$ )		
	micropore	mesopore	total	micropore	mesopore	total
ESH-P-B0	3.20	15.64	18.84	6.08	3.75	9.83
ESH-P-B3	4.76	12.45	17.21	10.11	3.83	13.94
ESH-P-B9	11.76	27.40	39.16	24.66	9.74	34.40
ESH-P-B24	5.20	13.88	19.08	12.44	4.25	16.70
HD1-B7	4.26	9.37	13.63	8.91	3.37	12.28
HD1-T4	1.53	6.01	7.54	3.82	1.52	5.34
HD1-T14	0.93	10.09	11.02	1.89	1.66	3.55
HD1-T24	1.18	7.32	8.50	2.21	1.45	3.66
SHP-B3	9.23	6.27	15.51	19.70	2.70	22.40
ESP-B6	4.99	14.17	19.16	9.21	4.86	14.07
ESP-B9	4.62	10.09	14.71	6.51	3.32	9.83
HQP-B6	3.48	35.60	39.07	6.04	7.20	13.24
HZP-B3	7.68	15.75	23.43	18.39	5.11	23.51
MHPP-B3	11.72	24.65	36.36	23.58	8.64	32.21
MHPP-B5	10.06	30.03	40.09	20.51	7.87	28.38
MHPP-B15	10.50	23.63	34.14	23.69	6.73	30.42

Pure and Applied Chemistry (IUPAC) classification of adsorption isotherms has six types; the Dalong Formation shale samples mainly exhibit type-IV isotherms, which indicate mesoporous adsorbent materials with a noticeable hysteresis loop. In the adsorption curve, the curve rises sharply when  $P/P_0 < 0.05$ , rises slowly when  $0.05 < P/P_0 < 0.95$ , and rises sharply again when  $P/P_0$  is close to 1.0. The adsorption and desorption curves do not overlap when  $P/P_0$  exceeds 0.45 because of capillary condensation, which creates a hysteresis loop. The curve plunges fast at a  $P/P_0$  of 0.5 and coincides with the adsorption curve at  $P/P_0$  below or equal to 0.45. For some samples (such as SHP-B3 and ESP-B9), there is no closure of the hysteresis loop at a relative pressure of 0.45.

The pore structure can be inferred from the hysteresis loop's shape. The Dalong Formation shale samples mostly fall into two categories of hysteresis loops: H2 and H3 (Figure 3), out of the four types defined by the IUPAC. Some shale samples have hysteresis loops with intermediate shapes that imply mixed pore

structures, and they cannot be clearly assigned to either H2 or H3.

The Dalong Formation shale samples exhibit different hysteresis loop types, reflecting their pore structures. Parallel-plate pores are present in samples ESH-P-B9, ESH-P-B24, HD1-B7, ESP-B6, HZP-B3, and MHPP-B3, as shown by their hysteresis loops that resemble those of type H2. On the other hand, samples ESH-P-B0, HD1-T4, HD1-T24, and HQP-B6 show hysteresis loops closer to type H3, suggesting that the pores are ink-bottle-shaped. Additionally, samples SHP-B3 and ESP-B9 exhibit unclosed hysteresis loops, indicating the presence of wedge- or cylinder-shaped pores. Mostly, samples ESH-P-B3, HD1-T14, and MHPP-B5 show type-H2 hysteresis loops with some type-H3 features, suggesting a combination of an ink-bottle and parallel-plate pores.

#### 4.4. Quantitative Characteristics of the Pore Structure.

The Dalong Formation shale samples had their pore structure analyzed by NLDFT. By use of the pore volume distribution and

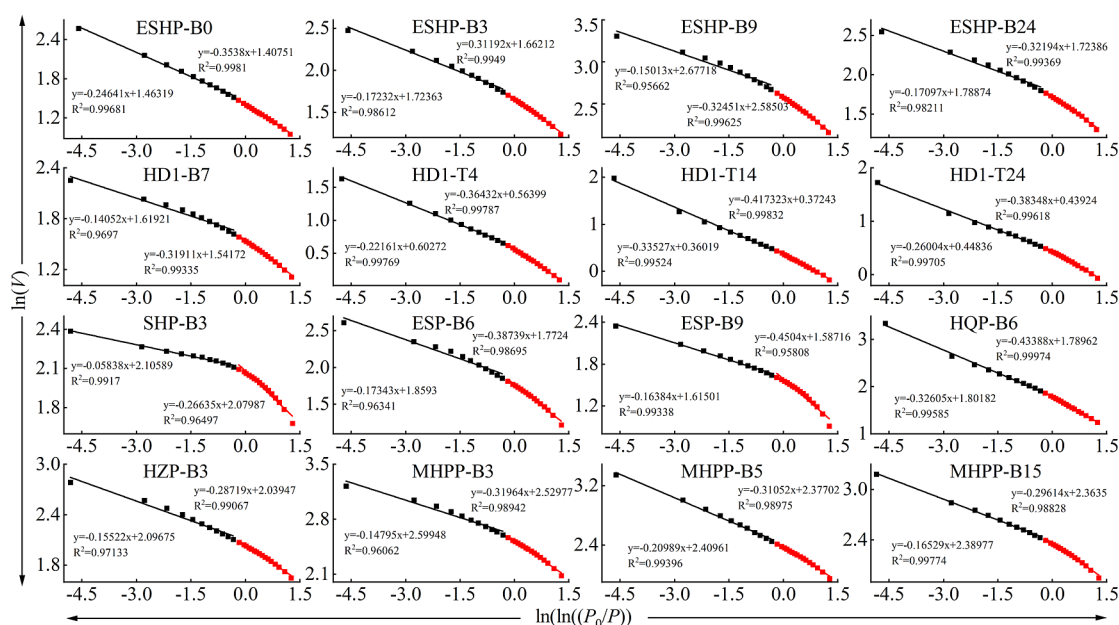


Figure 5. FHH model calculations for nitrogen adsorption data from Dalong Formation shales.

Table 3. Calculation Results of Fractal Dimension of Shale Samples from the Dalong Formation

sample	$P/P_0: 0-0.45$			$P/P_0: 0.45-1$		
	$k_1$	$D_1 = k_1 + 3$	$R^2$	$k_2$	$D_2 = k_2 + 3$	$R^2$
ESHP-B0	-0.3538	2.6462	0.9981	-0.24641	2.75359	0.99681
ESHP-B3	-0.31192	2.68808	0.9949	-0.17232	2.82768	0.98612
ESHP-B9	-0.32451	2.67549	0.99625	-0.15013	2.84987	0.95662
ESHP-B24	-0.32194	2.67806	0.99369	-0.17097	2.82903	0.98211
HD1-B7	-0.31911	2.68089	0.99335	-0.14052	2.85948	0.9697
HD1-T4	-0.22161	2.77839	0.99769	-0.22161	2.77839	0.99769
HD1-T14	-0.41723	2.58277	0.99832	-0.33527	2.66473	0.99524
HD1-T24	-0.38348	2.61652	0.99618	-0.26004	2.73996	0.99705
SHP-B3	-0.26635	2.73365	0.96497	-0.05838	2.94162	0.9917
ESP-B6	-0.38739	2.61261	0.98695	-0.17343	2.82657	0.96341
ESP-B9	-0.4504	2.5496	0.95808	-0.16384	2.83616	0.99338
HQP-B6	-0.4338	2.5662	0.99974	-0.32605	2.67395	0.99585
HZP-B3	-0.28719	2.71281	0.99067	-0.15522	2.84478	0.97133
MHPP-B3	-0.31964	2.68036	0.98942	-0.14795	2.85205	0.96062
MHPP-B5	-0.31052	2.68948	0.98975	-0.20989	2.79011	0.99396
MHPP-B15	-0.29614	2.70386	0.98828	-0.16529	2.83471	0.99774

the average pore diameter, the pore size distribution was determined. As Figure 4 shows, the 16 shale samples have different pore volume distributions. Most samples had a bimodal distribution of pore diameters, with peaks in the ranges of 0–2 and 2–5 nm. However, some samples, such as SHP-B3 and ESP-B9, showed a unimodal distribution. The samples HD1-T14, HD1-T24, and HQP-B6 had a wider pore size distribution, with the distribution curve fluctuating between 25 and 35 nm.

The SSA and pore volume of micropores and mesopores in the shale samples from the Dalong Formation were calculated and are presented in Table 2. The total SSA had a mean of 17.11 m<sup>2</sup>/g and varied from 3.55 to 34.40 m<sup>2</sup>/g. The majority of SSA was attributed to micropores, accounting for an average of 70%. The total pore volume varied from 7.54 to 40.10 cm<sup>3</sup>·g<sup>-1</sup> × 10<sup>-3</sup>, with an average of 17.11 cm<sup>3</sup>·g<sup>-1</sup> × 10<sup>-3</sup>. Mesopores dominated the pore volume, accounting for over 70%.

**4.5. Pore Fractal Characteristics.** Fractal dimensions can describe the porous structure and surface roughness of porous

materials. According to previous studies, there are several calculation methods for fractal dimension from gas adsorption data, including the fractal Brunauer–Emmett–Teller, FHH, NK, and WL models.<sup>48–50</sup> Among them, the FHH model is more reliable, and it has been used for sedimentary rocks.<sup>18,51</sup> The expression of the FHH model is

$$\ln V = k \ln \left( \ln \frac{P_0}{P} \right) + C \quad (1)$$

where  $V$  is the volume of adsorbed gas at equilibrium pressure  $P$ ,  $P_0$  is the saturation pressure,  $k$  is the slope of  $\ln(V)$  and  $\ln[\ln(P_0/P)]$ , and  $C$  is a constant.

According to the FHH fractal model, slope( $k$ ) of the fitting line on the  $\ln(V) - \ln[\ln(P_0/P)]$  plot gives the fractal dimension,  $D = k + 3$ , and the  $D$  value is between 2 and 3. Generally, surface smoothness decreases and irregularity increases with the  $D$  value, which shows complex surfaces.<sup>52</sup>

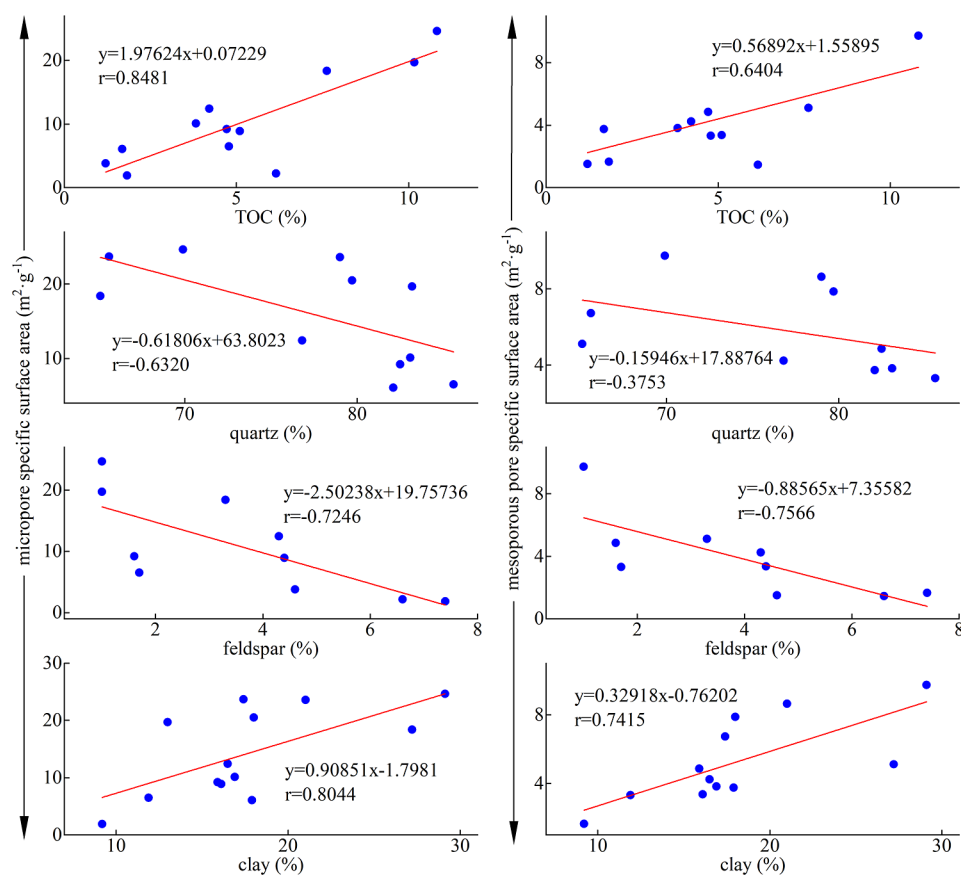


**Figure 6.** Correlations of pore SSA and mineral fraction.

The  $\ln(V) - \ln[\ln(P_0/P)]$  fitting curve for calculating the fractal dimension of the shale samples according to the FHH fractal model is shown in Figure 5. The plot has two distinct linear regions for each sample, corresponding to the nitrogen adsorption curve  $0 < P/P_0 < 0.45$  and  $0.45 < P/P_0 < 1.0$ . The end of the hysteresis loop at the point where  $P/P_0 = 0.45$  shows that the gas adsorption behavior varies in the two regions. Thus, the samples have different fractal dimensions in these regions, which are denoted as  $D_1$  and  $D_2$ . Table 3 shows the parameters used to calculate the fractal dimension of each sample with the FHH model. The linear fits have high accuracy ( $R^2 > 0.95$ ), which validates the reliability of the calculations. The average values of  $D_1$  and  $D_2$  for the shale pores of the Dalong Formation are 2.66 and 2.81, respectively, with  $D_1$  and  $D_2$  ranging between 2.55 and 2.78 and 2.66 and 2.94, respectively.

As shown in Table 3,  $D_2$  exceeds  $D_1$  for each sample. They do not have an obvious relationship, indicating that they correspond to two different fractal dimensions of the shale. This finding differs from the shale of the Wufeng–Longmaxi Formation in the Jiaoshiba area of the Sichuan Basin.<sup>53</sup> However, it is consistent with the Bakken shale in the USA.<sup>19</sup>

## 5. DISCUSSION

**5.1. Relationships between Mineral Composition and Pore Structure.** Figure 6 and Figure 7 demonstrate the impact of quartz, clay minerals, TOC content, and feldspar on the pore SSA values and pore volume of shale. A clear trend is observed: a higher TOC content leads to larger SSA and volume for both micropores and mesopores. The correlation coefficient between TOC and micropore SSA is higher than that between TOC and mesopore SSA. This is because TOC plays a crucial role in

creating nanoscale thermogenic pores in organic matter (Figure 2d), which dominate the micropore SSA and volume. As the amount of TOC grows, there are more nanoscale organic matter micropores in shale. These holes are smaller than 2 nm and made from pyrolysis of kerogen.

The SSA and volume of both micro- and mesopores decrease as the content of quartz and feldspar increases. During the early burial stage, large-grained quartz particles can protect larger pores from compaction, thus preserving the pore space. However, the filling of pores by authigenic biogenic quartz precipitates hinders pore preservation.<sup>39</sup> Previous studies have shown that the quartz in the Dalong Formation shale is mainly derived from biogenic sources,<sup>34</sup> and the pore development in the Dalong Formation shale is inhibited by quartz. Feldspar is susceptible to erosion by acidic fluids, resulting in the formation of pores. However, potassium feldspar has the ability to generate secondary minerals that can fill these intergranular pores,<sup>54</sup> thereby hindering pore development.

The pore SSA and volume of micropores and mesopores in shale are positively influenced by the presence of clay minerals. Clay minerals exhibit various crystal shapes, including flakes, fibers, and flocs, which facilitates the development of pores of different sizes.<sup>55</sup> These pore sizes associated with clay minerals are widely distributed, ranging from nanometers to micrometers.<sup>56</sup> However, due to their high plasticity and low hardness, clay minerals are prone to compaction. Compaction leads to the compression of larger pores, while the structural properties of clay minerals allow for the retention of smaller micropores and mesopores.<sup>57</sup> As a result, clay minerals ultimately promote the development of micropores and mesopores in shale.<sup>57,60</sup>

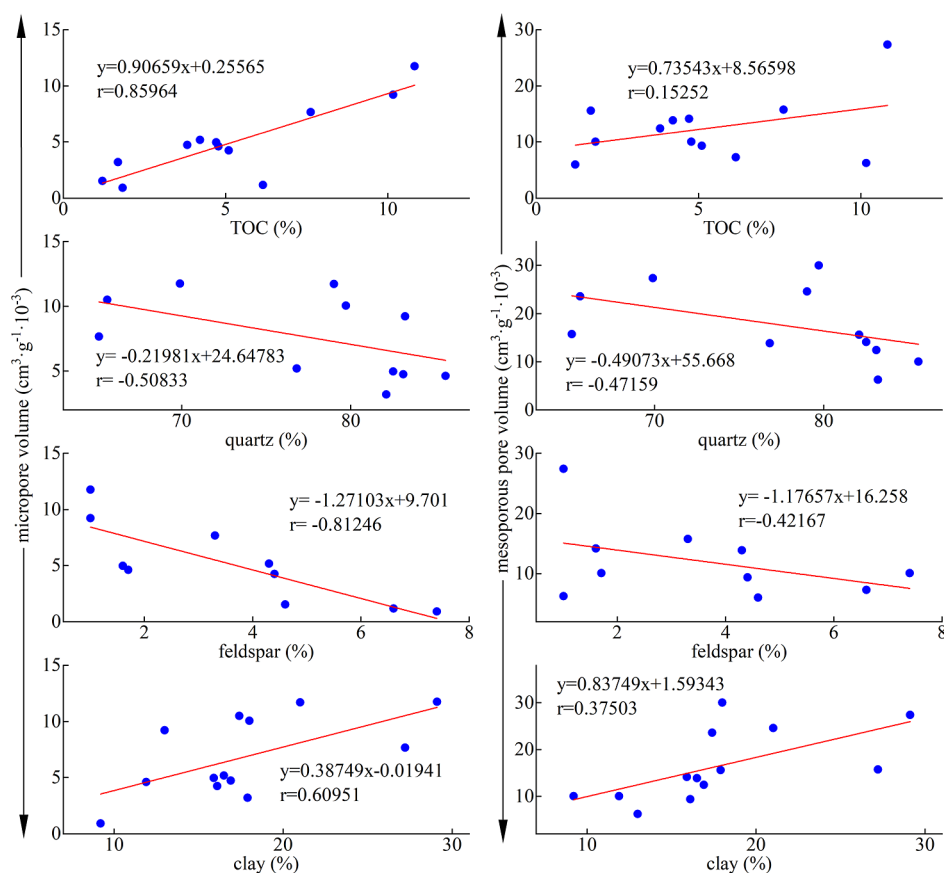


Figure 7. Correlations of pore volume and mineral fraction.

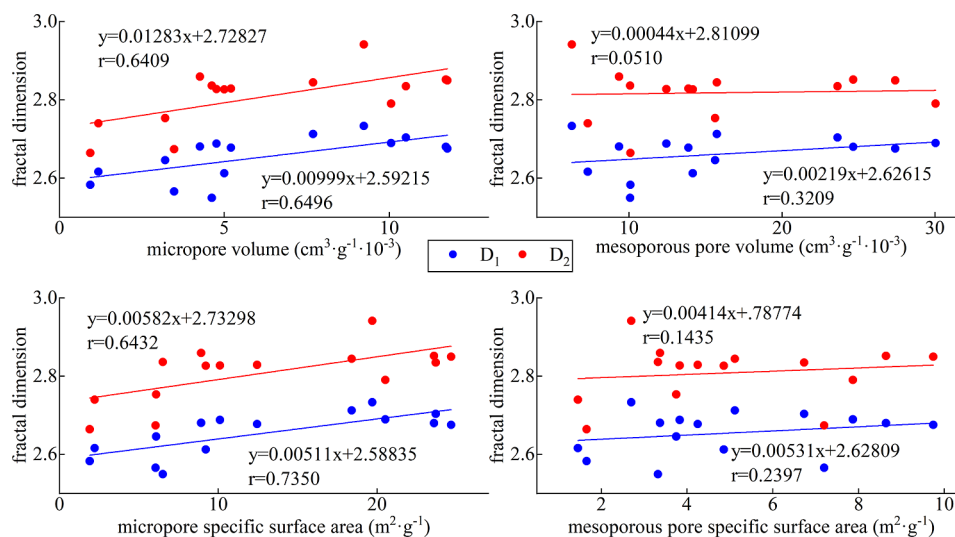
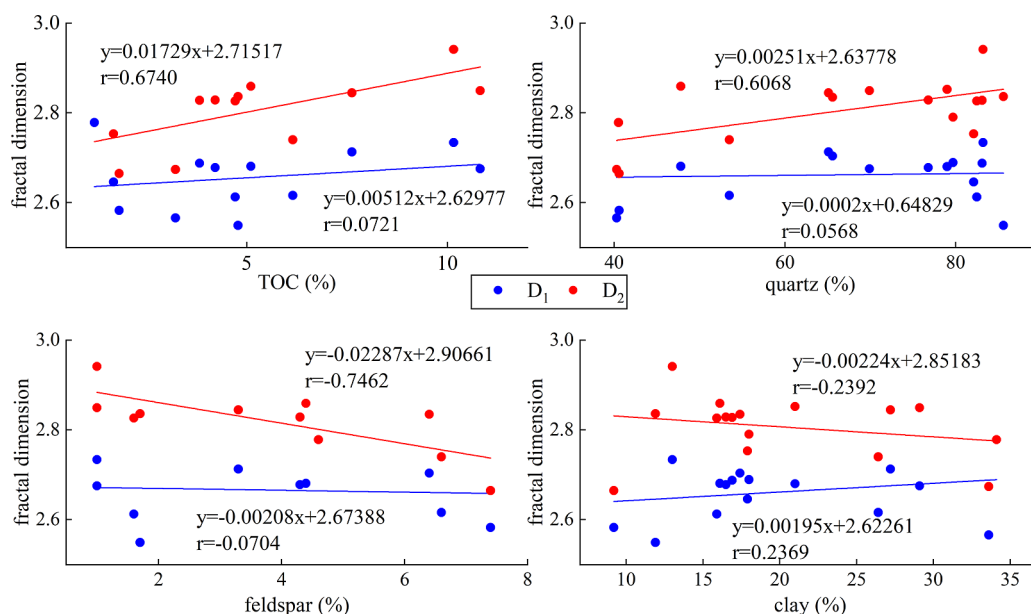


Figure 8. Plot of pore structure vs fractal dimension.

**5.2. Relationships between Pore Structure and Fractal Dimension.** How irregular the pore surfaces and structures are in porous materials is shown by the fractal dimension.  $D_1$  represents the fractal dimension of the pore surface. At this range, a one-molecule-thick layer is made on the pore surface by adsorption, which is mainly governed by the van der Waals force.  $D_2$  represents the fractal dimension of the pore structure. At this range, adsorption is dominated by capillary condensation and forms a multilayer in the pore space.<sup>58</sup>

The connection between  $D_1$ ,  $D_2$ , and the parameters of the shale pore structure is illustrated in Figure 8. Micropore volume and SSA growth raise both  $D_1$  and  $D_2$ , indicating that micropores are more irregular and complex. The correlation between micropore SSA and  $D_1$  ( $r = 0.7350$ ) is slightly stronger than the correlation between micropore volume and  $D_1$  ( $r = 0.6496$ ), suggesting that  $D_1$  is more sensitive to the unevenness of the pore surface. This finding is consistent with the research conducted by Yao et al. on North China coal.<sup>59</sup> The correlation coefficients of  $D_2$  with micropore SSA ( $r = 0.6409$ ) and



**Figure 9.** Plot of shale mineral fraction and TOC content against fractal dimension.

micropore volume ( $r = 0.6432$ ) are similar. Mesopore SSA and volume do not affect the fractal dimensions ( $D_1$  and  $D_2$ ) much, as they have no strong link, indicating that mesopore development has little impact on the fractal dimension.

**5.3. Factors Affecting the Fractal Dimension.** To investigate the factors affecting the fractal dimension, we mainly focus on the effect of shale's main minerals and TOC content on fractal dimension, and the related graph is displayed in Figure 9.

The  $D_2$  value of shale increases as the TOC content increases, showing a positive correlation ( $r = 0.674$ ). This suggests that the TOC has a beneficial impact on the fractal dimension. Shale contains numerous nanoscale organic matter pores (Figure 3). A higher TOC content makes shale micropores SSA bigger and the pore structure more complex. This increases the fractal dimension of the pore space.

The fractal dimension of shale pores is influenced by the origin of the quartz. The quartz content in the transitional shale has little effect on the pore fractal dimension.<sup>22</sup> The fractal dimension of the Lower Cambrian Qiongzhusi shale in eastern Yunnan decreases with quartz content.<sup>60</sup> Terrigenous input is the main source of quartz in this shale. Conversely, the fractal dimension of the Longmaxi shale in southern Sichuan goes up with quartz content, which partly originates from siliceous organisms.<sup>61</sup> In this study, the  $D_2$  value is positively correlated with shale's quartz content ( $r = 0.6068$ ). The quartz in the Dalong Formation shale is primarily an authigenic quartz. Unlike detrital quartz that existed before diagenesis, authigenic quartz fills the original shale pores in a microcrystalline form. While reducing the shale porosity, the irregular morphology of authigenic quartz leads to an increased complexity of shale pores, resulting in an overall increase in fractal dimension.

The  $D_2$  value decreases as the feldspar content increases, showing a negative correlation ( $r = -0.7462$ ). This suggests that the presence of feldspar not only reduces the pore volume and SSA but also simplifies the pore structure of shale. Feldspar is chemically unstable and easily corrodes and is dissolved by organic acids. This results in small pore blockage and pore SSA and volume reduction.<sup>62</sup> Additionally, the development of feldspar cleavage promotes the formation of larger cleavage

fractures, which increases the connectivity between the pores and the development of larger pores. Therefore, the increase in the feldspar content makes the pore structure simpler and the fractal dimension lower.

On the other hand, the increase in clay mineral content has a minimal effect on the  $D_2$  value; however, SSA and micropore volume increase with it, indicating that clay minerals affect pore development in a complex way. Clay minerals have a structure that creates many pores inside and between grains, which increases SSA and pore volume. However, the strong plasticity of clay minerals leads to stronger shale compaction during diagenesis,<sup>63</sup> making the shale denser and reducing the proportion and connectivity of pores. This ultimately results in a decrease in the pore structure complexity.

There is a low correlation between the  $D_1$  values and mineral components, which means that mineral content changes have little impact on the  $D_1$  values. Further research is needed to identify the factors that influence the  $D_1$  value.

## 6. CONCLUSIONS

This study examines the pore morphology of shale in the Dalong Formation using SEM. Shale pore fractals are studied using nitrogen adsorption and FHH fractal theory. How shale composition and pore structure affect fractal dimensions and what factors determine it were analyzed. The main findings are as follows:

- (1) Intragranular, intergranular, and organic matter pores, along with some microfractures, make up most of the shale pores in the Dalong Formation. Nitrogen adsorption results show that the pore shapes are primarily parallel-plate-like and ink-bottle-like, exhibiting clear fractal features.
- (2) The pore structure gets more complex as the micropores grow. This is reflected by the fractal dimension and the volume and SSA of micropores being positively related. As the micropores develop more, the fractal dimension increases.
- (3) The pore structure becomes more complex when the shale samples have more micropores due to higher TOC

content. However, the fractal dimension is hardly influenced by clay minerals, which enhance the pore SSA and micropore volume. The effects of quartz and feldspar on pores and fractal dimension are opposite in the shale of the Dalong Formation. The correlation between fractal dimension  $D_2$  and quartz content is positive, while the correlation between fractal dimension  $D_2$  and feldspar content is negative.

## AUTHOR INFORMATION

### Corresponding Author

**Weiqing Liu** – School of Resources and Environment, Henan Polytechnic University, Jiaozuo 454003, China; Chengdu Institute of Geology and Mineral Resources, Chengdu 610081, China; [orcid.org/0000-0001-5783-4573](https://orcid.org/0000-0001-5783-4573);  
Email: [weiqingliu@hpu.edu.cn](mailto:weiqingliu@hpu.edu.cn)

### Authors

**Qiang Zhu** – School of Resources and Environment, Henan Polytechnic University, Jiaozuo 454003, China

**Yu Qiao** – School of Resources and Environment, Henan Polytechnic University, Jiaozuo 454003, China; [orcid.org/0000-0003-0708-7500](https://orcid.org/0000-0003-0708-7500)

**Jienan Pan** – School of Resources and Environment, Henan Polytechnic University, Jiaozuo 454003, China; [orcid.org/0000-0001-7995-0129](https://orcid.org/0000-0001-7995-0129)

**Wei Wu** – School of Resources and Environment, Henan Polytechnic University, Jiaozuo 454003, China

**Luqi Chen** – School of Resources and Environment, Henan Polytechnic University, Jiaozuo 454003, China

Complete contact information is available at:

<https://pubs.acs.org/10.1021/acsomega.3c09085>

### Notes

The authors declare no competing financial interest.

The authors confirm that the data supporting the findings of this study are available within the article.

All authors certify that they have no affiliations with or involvement in any organization or entity with any financial interest or nonfinancial interest in the subject matter or materials discussed in this manuscript.

## ACKNOWLEDGMENTS

The research was supported by the National Natural Science Foundations of China (no. 42002031).

## REFERENCES

- (1) Bellani, J.; Verma, H. K.; Khatri, D.; Makwana, D.; Shah, M. Shale gas: a step toward sustainable energy future. *J. Pet. Explor. Prod. Technol.* **2021**, *11* (5), 2127–2141.
- (2) Shirazi, M.; Ghasemi, A.; Šimurina, J. The impact of the North American shale gas technology on the US' energy security: the case of natural gas. *Int. J. Sustainable Energy* **2022**, *41* (7), 810–831.
- (3) Feng, Z.; Hao, F.; Tian, J.; Zhou, S.; Dong, D.; Huang, S. Shale gas geochemistry in the Sichuan Basin, China. *Earth-Sci. Rev.* **2022**, *232*, 104141.
- (4) Zhang, P.; Lu, S.; Li, J.; Wang, J.; Zhang, J.; Chen, G.; Huang, H.; Zhi, Q.; Yin, Y. Microscopic characteristics of pore-fracture system in lacustrine shale from Dongying Sag, Bohai Bay Basin, China: Evidence from scanning electron microscopy. *Mar. Pet. Geol.* **2023**, *150*, 106156.
- (5) Pang, X.; Jia, C.; Chen, J.; Li, M.; Wang, W.; Hu, Q.; Guo, Y.; Chen, Z.; Peng, J.; Liu, K.; et al. A unified model for the formation and distribution of both conventional and unconventional hydrocarbon reservoirs. *Geosci. Front.* **2021**, *12* (2), 695–711.
- (6) Zhu, H.; Ju, Y.; Lu, W.; Han, K.; Qi, Y.; Neupane, B.; Sun, Y.; Cai, J.; Xu, T.; Huang, C.; et al. The Characteristics and Evolution of Micro-Nano Scale Pores in Shales and Coals. *J. Nanosci. Nanotechnol.* **2017**, *17* (9), 6124–6138.
- (7) Chandra, D.; Bakshi, T.; Bahadur, J.; Hazra, B.; Vishal, V.; Kumar, S.; Sen, D.; Singh, T. N. Pore morphology in thermally-treated shales and its implication on CO<sub>2</sub> storage applications: A gas sorption, SEM, and small-angle scattering study. *Fuel* **2023**, *331*, 125877.
- (8) Zheng, A.; Bao, H.; Liu, L.; Tu, M.; Hu, C.; Yang, L. Investigation of Multiscaled Pore Structure of Gas Shales using Nitrogen Adsorption and FE-SEM Imaging Experiments[J]. *Geofluids* **2022**, *2022*, 1057653.
- (9) Mandelbrot, B. How Long Is the Coast of Britain? Statistical Self-Similarity and Fractional Dimension[J]. *Science* **1967**, *156* (3775), 636–638.
- (10) Avnir, D.; Farin, D.; Pfeifer, P. Surface geometric irregularity of particulate materials: The fractal approach. *J. Colloid Interface Sci.* **1985**, *103* (1), 112–123.
- (11) Krohn, C. E.; Thompson, A. H. Fractal sandstone pores: Automated measurements using scanning-electron-microscope images. *Phys. Rev. B* **1986**, *33* (9), 6366–6374.
- (12) Yao, Y.; Liu, D.; Tang, D.; Tang, S.; Huang, W.; Liu, Z.; Che, Y. Fractal characterization of seepage-pores of coals from China: An investigation on permeability of coals. *Comput. Geosci.* **2009**, *35* (6), 1159–1166.
- (13) Zhang, S.; Tang, S.; Tang, D.; Huang, W.; Pan, Z. Determining fractal dimensions of coal pores by FHH model: Problems and effects. *J. Nat. Gas Sci. Eng.* **2014**, *21*, 929–939.
- (14) Wang, F.; Li, S. Determination of the Surface Fractal Dimension for Porous Media by Capillary Condensation. *Ind. Eng. Chem. Res.* **1997**, *36* (5), 1598–1602.
- (15) Liu, K.; Ostadhassan, M.; Kong, L. Fractal and Multifractal Characteristics of Pore Throats in the Bakken Shale. *Transp. Porous Media* **2019**, *126* (3), 579–598.
- (16) Liu, K.; Ostadhassan, M.; Jang, H. W.; Zakharova, N. V.; Shokouhimehr, M. Comparison of fractal dimensions from nitrogen adsorption data in shale via different models. *RSC Adv.* **2021**, *11* (4), 2298–2306.
- (17) Liu, X.; Jin, Z.; Lai, J.; Fan, X.; Guan, M.; Shu, H.; Wang, G.; Liu, M.; Luo, Y. Fractal behaviors of NMR saturated and centrifugal T<sub>2</sub> spectra in oil shale reservoirs: The Paleogene Funing formation in Subei basin, China. *Mar. Pet. Geol.* **2021**, *129*, 105069.
- (18) Yang, F.; Ning, Z.; Liu, H. Fractal characteristics of shales from a shale gas reservoir in the Sichuan Basin, China. *Fuel* **2014**, *115*, 378–384.
- (19) Liu, K.; Ostadhassan, M.; Zhou, J.; Gentzis, T.; Rezaee, R. Nanoscale pore structure characterization of the Bakken shale in the USA. *Fuel* **2017**, *209*, 567–578.
- (20) Hazra, B.; Wood, D. A.; Vishal, V.; Varma, A. K.; Sakha, D.; Singh, A. K. Porosity controls and fractal disposition of organic-rich Permian shales using low-pressure adsorption techniques. *Fuel* **2018**, *220*, 837–848.
- (21) Yang, R.; He, S.; Yi, J.; Hu, Q. Corrigendum to “Yang, R., He, S., Yi, J., Hu, Q., 2016. Nano-scale pore structure and fractal dimension of organic-rich Wufeng-Longmaxi shale from Jiaoshiba area, Sichuan Basin: Investigations using FE-SEM, gas adsorption and helium pycnometry” [*Mar. Pet. Geol.* *70* 27–45]. *Mar. Pet. Geol.* **2020**, *114*, 104167.
- (22) Li, Y.; Wang, Z.; Pan, Z.; Niu, X.; Yu, Y.; Meng, S. Pore structure and its fractal dimensions of transitional shale: A cross-section from east margin of the Ordos Basin, China. *Fuel* **2019**, *241*, 417–431.
- (23) Zhang, J.; Shi, M.; Wang, D.; Tong, Z.; Hou, X.; Niu, J.; Li, X.; Li, Z.; Zhang, P.; Huang, Y. Fields and directions for shale gas exploration in China[J]. *Nat. Gas Ind.* **2021**, *41* (08), 69–80. (In Chinese)
- (24) Tian, G. An important discovery of shale gas was obtained in the Permian Dalong Formation in western Hubei.[J]. *Nat. Gas Ind.* **2021**, *41* (06), 51. (In Chinese)
- (25) Wang, Q.; Lu, H.; Wang, T.; Liu, D.; Peng, P.; Zhan, X.; Li, X. Pore characterization of Lower Silurian shale gas reservoirs in the Middle Yangtze region, central China. *Mar. Pet. Geol.* **2018**, *89*, 14–26.

- (26) Wang, Q.; Wang, T.; Liu, W.; Zhang, J.; Feng, Q.; Lu, H.; Peng, P. Relationships among composition, porosity and permeability of Longmaxi Shale reservoir in the Weiyuan Block, Sichuan Basin, China. *Mar. Pet. Geol.* **2019**, *102*, 33–47.
- (27) Xi, Z.; Tang, S.; Lash, G. G.; Ye, Y.; Lin, D.; Zhang, B. Depositional controlling factors on pore distribution and structure in the lower Silurian Longmaxi shales: Insight from geochemistry and petrology. *Mar. Pet. Geol.* **2021**, *130*, 105114.
- (28) Chen, K.; Yang, R.; Bao, H.; Dong, T.; Jia, A.; Hu, Q.; Guo, X.; He, S. Depositional-diagenetic process and their implications for pore development of Wufeng-Longmaxi shales in the Jiangdong block, Fuling shale gas field, SW China. *Mar. Pet. Geol.* **2023**, *151*, 106177.
- (29) Xu, L.; Liu, Z.; Zhang, Y.; Qiu, Y.; Duan, K. Shale Gas Reservoir Potential Evaluation of Dalong Formation in Hefeng of Western Hubei Province[J]. *Spec. Oil Gas Reservoirs* **2018**, *25* (02), 13–18. (In Chinese)
- (30) Wang, D.; Yu, J.; Chen, W.; Zhou, X.; Zhang, Y.; Xu, L.; Zhou, B.; Leng, S.; Jia-Qi, H. Characteristics of Shale Reservoir and Resource Potential Evaluation in the Upper Permian Dalong Formation of Hefeng area in Western of Hubei Province[J]. *South China Geol.* **2020**, *36* (01), 9–18. (In Chinese)
- (31) Cao, T.; Liu, H.; Pan, A.; Fu, Y.; Deng, M.; Cao, Q.; Huang, Y.; Yu, Y. Pore evolution in siliceous shales and its influence on shale gas-bearing capacity in eastern Sichuan-western Hubei, China. *J. Petrol. Sci. Eng.* **2022**, *208*, 109597.
- (32) Wei, Z.; Wang, Y.; Wang, G.; Sun, Z.; Zhang, T.; Xu, L.; Ma, X.; He, W. Paleoenvironmental conditions of organic-rich Upper Permian Dalong Formation shale in the Sichuan Basin, southwestern China. *Mar. Pet. Geol.* **2018**, *91*, 152–162.
- (33) Wang, Y.; Bai, L.; Zhang, Y.; Zhang, X.; Yang, B.; Duan, K.; Wang, Y.; Xie, T. Reservoir Characteristics and Influencing Factors of Organic-Rich Siliceous Shale of the Upper Permian Dalong Formation in Western Hubei. *Energies* **2023**, *16* (13), 5130.
- (34) Wu, W.; Liu, W.; Mou, C.; Liu, H.; Qiao, Y.; Pan, J.; Ning, S.; Zhang, X.; Yao, J.; Liu, J. Organic-rich siliceous rocks in the upper Permian Dalong Formation (NW middle Yangtze): Provenance, paleoclimate and paleoenvironment. *Mar. Pet. Geol.* **2021**, *123*, 104728.
- (35) Feng, Z.; Li, S.; Yang, Y.; Ji, Z. Potential of oil and gas of the Permian of south China from the viewpoint of lithofacies paleogeography[J]. *Acta Pet. Sin.* **1997**, *18* (1), 10.
- (36) Yin, H.; Jiang, H.; Xia, W.; Feng, Q.; Zhang, N.; Shen, J. The end-Permian regression in South China and its implication on mass extinction. *Earth-Sci. Rev.* **2014**, *137*, 19–33.
- (37) Feng, Z.; He, Y.; Wu, S. Lithofacies Paleogeography of Permian Middle and Lower Yangtze Region[J]. *Acta Sedimentol. Sin.* **1993**, No. 3, 13–24. (In Chinese)
- (38) Zavattieri, A. M.; Gutiérrez, P. R.; Ezpeleta, M. *Syndesmorion stellatum* (Fijalkowska) Foster et Afonin chlorophycean algae and associated microphytoplankton from lacustrine successions of the La Veteada Formation (late Permian), Paganzo Basin, Argentina. Paleoenvironmental interpretations and stratigraphic implications. *Rev. Palaeobot. Palynol.* **2017**, *242*, 1–20.
- (39) Gao, P.; Xiao, X.; Meng, G.; Lash, G. G.; Li, S.; Han, Y. Quartz types and origins of the Upper Permian Dalong Formation shale of the Sichuan Basin: Implications for pore preservation in deep shale reservoirs. *Mar. Pet. Geol.* **2023**, *156*, 106461.
- (40) Li, S.; Li, Y.; He, Z.; Chen, K.; Zhou, Y.; Yan, D. Differential deformation on two sides of Qiyueshan Fault along the eastern margin of Sichuan Basin, China, and its influence on shale gas preservation. *Mar. Pet. Geol.* **2020**, *121*, 104602.
- (41) He, Y.; Luo, J. Lithofacies palaeogeography of the Late Permian Changxing Age in Middle and Upper Yangtze Region[J]. *J. Palaeogeogr.* **2010**, No. 5, 497–514. (In Chinese)
- (42) Zheng, B.; Mou, C.; Wang, X.; Chen, H.; Xiao, Z. Paleoclimate and paleoceanographic evolution during the Permian-Triassic transition (western Hubei area, South China) and their geological implications. *Palaeogeogr. Palaeoclimatol. Palaeoecol.* **2021**, *564*, 110166.
- (43) Liu, W.; Yao, J.; Tong, J.; Qiao, Y.; Chen, Y. Organic matter accumulation on the Dalong Formation (Upper Permian) in western Hubei, South China: Constraints from multiple geochemical proxies and pyrite morphology. *Palaeogeogr. Palaeoclimatol. Palaeoecol.* **2019**, *514*, 677–689.
- (44) Guo, X.; Hu, D.; Huang, R.; Wei, Z.; Duan, J.; Wei, X.; Fan, X.; Miao, Z. Deep and ultra-deep natural gas exploration in the Sichuan Basin: Progress and prospect. *Nat. Gas Ind.* **2020**, *7* (5), 419–432.
- (45) Xu, L.; Zhang, Y.; Chen, C.; Zhou, X.; Wen, Y. Shale Gas Reservoir and Gas-Bearing Properties of Wufeng-Longmaxi Formations in the Periphery of Huangling Anticline of Western Hubei Province[J]. *Spec. Oil Gas Reservoirs* **2019**, *26* (05), 26–32. (In Chinese)
- (46) Milliken, K. L.; Rudnicki, M.; Awwiller, D. N.; Zhang, T. Organic matter-hosted pore system, Marcellus Formation (Devonian), Pennsylvania. *AAPG Bull.* **2013**, *97* (2), 177–200.
- (47) Xie, W.; Wang, M.; Wang, H.; Ma, R.; Duan, H. Diagenesis of shale and its control on pore structure, a case study from typical marine, transitional and continental shales. *Front. Earth Sci.* **2021**, *15* (2), 378–394.
- (48) Fripiat, J. J.; Gattineau, L.; Van Damme, H. Multilayer physical adsorption on fractal surfaces. *Langmuir* **1986**, *2* (5), S62–S67.
- (49) Mahamud, M. M.; Novo, M. F. The use of fractal analysis in the textural characterization of coals. *Fuel* **2008**, *87* (2), 222–231.
- (50) Cai, Y.; Liu, D.; Pan, Z.; Yao, Y.; Li, J.; Qiu, Y. Pore structure and its impact on CH<sub>4</sub> adsorption capacity and flow capability of bituminous and subbituminous coals from Northeast China. *Fuel* **2013**, *103*, 258–268.
- (51) Wang, Y.; Zhu, Y.; Liu, S.; Zhang, R. Pore characterization and its impact on methane adsorption capacity for organic-rich marine shales. *Fuel* **2016**, *181*, 227–237.
- (52) Reich, M. H.; Snook, I. K.; Wagenfeld, H. K. A fractal interpretation of the effect of drying on the pore structure of Victorian brown coal. *Fuel* **1992**, *71* (6), 669–672.
- (53) Yang, R.; He, S.; Yi, J.; Hu, Q. Nano-scale pore structure and fractal dimension of organic-rich Wufeng-Longmaxi shale from Jiaoshiba area, Sichuan Basin: Investigations using FE-SEM, gas adsorption and helium pycnometry. *Mar. Pet. Geol.* **2016**, *70*, 27–45.
- (54) Zhang, Y.; Pan, H.; Bai, Y.; Chen, G.; Luo, J.; Zhang, Y. Pore Characteristics, Oil Contents and Factors Influencing Laminated Shale in the First Member of the Qingshankou Formation in the Gulong Sag, Northern Songliao Basin. *Minerals* **2023**, *13* (9), 1220.
- (55) Wang, G.; Jin, Z.; Zhang, Q.; Zhu, R.; Tang, X.; Liu, K.; Dong, L. Effects of clay minerals and organic matter on pore evolution of the early mature lacustrine shale in the Ordos Basin, China. *J. Asian Earth Sci.* **2023**, *246*, 105516.
- (56) Zhu, H.; Li, S.; Hu, Z.; Ju, Y.; Pan, Y.; Yang, M.; Lu, Y.; Wei, M.; Qian, W. Microstructural observations of clay-hosted pores in black shales: implications for porosity preservation and petrophysical variability. *Clay Miner.* **2023**, *58* (3), 310–323.
- (57) Hucheng, D.; Meiyang, F.; Wen, Z.; Liying, Z.; Xinhui, X.; Yilin, L.; Dailun, W. The pores evolution of lacustrine shale induced by smectite-to-illite conversion and hydrocarbon generation: upper Triassic Yanchang Formation, Ordos Basin, China. *J. Petrol. Sci. Eng.* **2021**, *202*, 108460.
- (58) Pyun, S.; Rhee, C. An investigation of fractal characteristics of mesoporous carbon electrodes with various pore structures. *Electrochim. Acta* **2004**, *49* (24), 4171–4180.
- (59) Yao, Y.; Liu, D.; Tang, D.; Tang, S.; Huang, W. Fractal characterization of adsorption-pores of coals from North China: An investigation on CH<sub>4</sub> adsorption capacity of coals. *Int. J. Coal Geol.* **2008**, *73* (1), 27–42.
- (60) Li, A.; Ding, W.; He, J.; Dai, P.; Yin, S.; Xie, F. Investigation of pore structure and fractal characteristics of organic-rich shale reservoirs: A case study of Lower Cambrian Qiongzhusi formation in Malong block of eastern Yunnan Province, South China. *Mar. Pet. Geol.* **2016**, *70*, 46–57.
- (61) Liang, L.; Xiong, J.; Liu, X. Fractal characteristics of pore structure of Longmaxi Formation shale in south of Sichuan Basin, China[J]. *J. Chengdu Univ. Technol. (Sci. Technol. Ed.)* **2015**, *42* (06), 700–708. (In Chinese)

(62) An, C.; Liu, G.; Sun, M.; You, F.; Wang, Z.; Cao, Y. Analysis of shale pore structure characteristics based on nitrogen adsorption experiment and fractal FHH model: a case study of 7th member of Triassic Yanchang Formation in Huachi area, Ordos Basin[J]. *Pet. Geol. Exp.* **2023**, *45* (03), 576–586. (In Chinese)

(63) Zhao, D.; Guo, Y.; Zhu, Y.; Wang, G.; Chong, X.; Hu, X. Analysis of micro-scale heterogeneity characteristics in marine shale gas reservoir: Pore heterogeneity and its quantitative characterization[J]. *J. China Inst. Min. Technol.* **2018**, *47* (02), 296–307. (In Chinese)